Spatial Convergence of Bidirectional Reflectance Models

JOHN M. DAVIS AND STEPHEN K. COX

Department of Atmospheric Science, Colorado State University, Fort Collins, Colorado

(Manuscript received 9 May 1997, in final form 17 November 1997)

ABSTRACT

Analyses of bidirectional reflectance data are presented with implications regarding the spatial scales appropriate for inferring irradiances from radiances reflected by various surface–atmosphere scenes. Multiple-angle radiance data collected in a nearly simultaneous manner during the 1979 Summer Monsoon Experiment are analyzed using the squared coherency statistic to suggest a method to deduce the minimum spatial scale appropriate for irradiance inferences. Spatial convergence of the irradiances inferred from the component radiances is presented as a function of averaging distance to imply magnitudes of errors that may result from use of ''similar scene'' bidirectional reflectance models. The reduction in the inference errors with an increasing number of angular viewing positions is also presented. The data are analyzed in search of preferred viewing directions with the result that little improvement is imparted to the inference by viewing the scenes from any specific view direction.

1. Introduction

The use of bidirectional reflectance models for inferring the reflected solar radiation flux density from narrow field of view (FOV) measurements is a critical process in the effort to monitor the earth's climate system from space. Efforts to categorize the angular patterns of solar radiation reflected from various components of the earth's atmosphere system have been numerous and have spanned the entire history of meteorological satellites. While wide FOV detectors can most accurately sample the total flux density at a particular point some hundreds of kilometers above the surface of the earth, these measurements do not lend themselves to monitoring the climate on a regional or local basis without the aid of angular models that specify the approximate angular distribution of the incoming signal. Narrow FOV instruments are intrinsically dependent on bidirectional reflectance (BDR) models to infer reflected flux densities from their limited sampling of the total angular space. The purpose of this paper is to provide some insight into the statistical features of the inference process for use as guidance in the use of BDR models.

As mentioned above, BDR models have been a necessary component in the interpretation of satellite flux density measurements. Some of the earliest efforts utilized measurements over various surfaces using Television Infrared Observation Satellite (TIROS) and Nimbus-type instruments carried aloft to altitudes of over 30 km by balloon-borne platforms, as reported by Bartman (1968). Early use of aircraft-borne instrumentation was reported on by Salomonson and Marlatt (1968), who used data from the *Nimbus-3* medium-resolution radiometer flown at an altitude of 3 km over stratus clouds. Of the several studies that followed, we mention here one of the most comprehensive and relatively recent efforts that compiled models for use in the Earth Radiation Budget Experiment described in Suttles et al. (1988) and those developed by Minnis and Harrison (1984), for use with the Geostationary Operational Environmental Satellite (GOES) platforms. In the future, use of BDR models will continue to play an important role in interpretation of the next generation of satellite observing systems, which are discussed in Wielicki et al. (1995).

Even though great care is taken to compile the BDR models, the accuracy of the inferences derived through their use is difficult to establish. Typically, statistics of the variability of the radiances used in constructing the models are calculated as an indication of how well they may perform, and averaging over latitude, longitude, and time is relied upon to reduce the discrepancies imparted to the inferences, which have been primarily used in climatic applications. If it is desired to use the inference process over smaller time- and/or space scales, then a more rigorous verification process is dictated since errors are less likely to average out. Ideally, the models would be checked by using them to make inferences of flux densities that are independently measured using instruments with hemispheric fields of view in a direct comparison. Also, although the BDR models

Corresponding author address: Dr. John M. Davis, Department of Atmospheric Science, Colorado State University, Fort Collins, CO 80523-1371.
E-mail: jmdavis@lamar.colostate.edu

are compiled using radiances reflected from similar scene types, they usually are composed of averages from sets of data taken at different times and from different locations. Thus, it is not entirely clear how to determine the minimum spatial extent of the regions to which they may be accurately applied. The purpose of the current work is to attempt to impart some appreciation of the nature of spatial convergence of BDR models and to suggest a method by which more confidence may be placed in their use over regional scale scenes.

2. Background

Another of the BDR model compilation efforts was conducted during 1979 MONEX (Monsoon Experiment). During MONEX, part of the activity consisted of aircraft flights by the National Aeronautics and Space Administration's Convair 990, which flew missions over the Rub'al Khali Desert of Saudi Arabia, the Arabian Sea, and the Indian subcontinent, including the Himalayan Mountains. By including data collected on ferry missions, it was possible to categorize 30 BDR models based on the type of reflecting medium and the value of the solar zenith angle; see Davis and Cox (1982). Included in the initial analysis were examinations of convergence features for some of the BDR models; however, these results were not published. As efforts are made to use flux densities inferred from satellite radiances on smaller time- and space scales, this analysis may provide some guidance, and it is for this reason that they are now being presented. It is noted at the outset that the data processing was conducted shortly after the MONEX campaign.

The prominent feature of the BDR effort during MONEX is the nature of the instrument used to collect the data. The instrument consisted of 13 photodiodes pointing in fixed directions with respect to the aircraft. The detector signals were sampled once each second, providing a nearly instantaneous sampling of the upwelling radiance field. The detectors were high quality silicon photodiodes (EG&G model SGD-100A) mounted in an aluminum housing that also contained high-grade operational amplifier circuits. The instrument, which became known as the ''bugeye,'' was roughly the size of a typical pyranometer and was mounted on the underside of the CV-990 next to the Eppley radiometers. No spectral filtering was employed, resulting in a broadband (0.4–1.1 μm) measurement of the upwelling radiances weighted by the silicon diode response function. The FOV of each detector was 10°, and the CV-990 flew typically at an altitude of from 10 to 12 km at a speed of 0.2 km s^{-1}. One of the photodiodes viewed the underlying scene pointing at nadir and four viewed the scene at 30° from nadir arranged every 90° in azimuth, with one of these viewing the forward direction of the aircraft. The remaining detectors were oriented at 60° from nadir in 45° increments of azimuth, again with one diode aligned in the forward direction. Figure 1 is a photograph of the instrument.

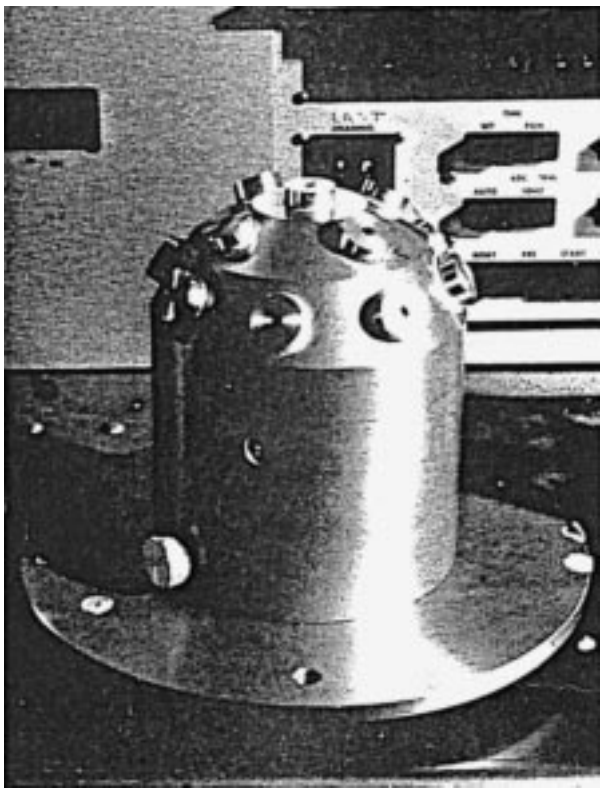

FIG. 1. Photograph of the multidetector instrument.

Thus, it was possible to sample the radiance fields from which the flux density or irradiance field was synthesized at a reasonably rapid rate, and it is this feature that allowed statistical analysis of the inference process. Note that the results presented below do not depend on absolute calibrations; rather, only relative calibrations are required. In some cases, even this requirement may be relaxed to maintenance of relative calibrations over a period of an hour or less during which data from a 600-km flight track are examined.

3. The inference model

The basic quantity that is normally used to perform the inference from the radiance to flux density was originally called the bidirectional reflectance normalization coefficient

$$\Psi(\theta, \phi, \theta_0) = \frac{\int_\Omega N(\theta, \phi, \theta_0) \cos\theta \, d\Omega}{\pi N(\theta, \phi, \theta_0)},$$

where θ and ϕ represent the nadir and relative azimuth angles of the observation, N represents the radiance reflected from surface on which solar radiation is incident at a zenith angle θ_0, and Ω represents the solid angle

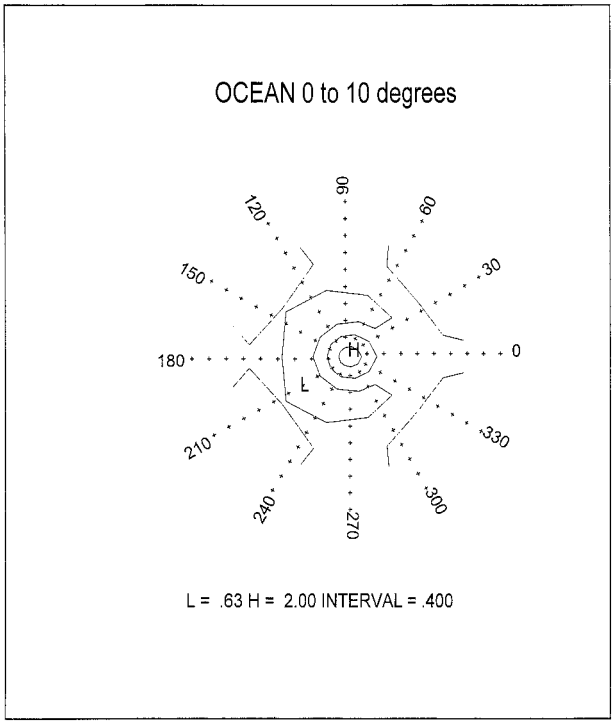

FIG. 2. Clear ocean BDR model for the 0°–10° solar zenith angle range.

of the upper hemisphere. Thus, an inference of the reflected flux density is obtained by assuming such a model, measured a priori, is representative for all such points at which the flux density is desired and that it may be obtained by multiplying a measured radiance by the product ($\Psi\pi$). Actually, it is usually the inverse of Ψ that is discussed since this quantity, which from here on will be referred to as the BDR model, is a normalized reflected radiance that is more easily visualized. For example, Fig. 2 displays the BDR model of the clear ocean scene for a solar zenith angle range from 0° to 10°. In it contours of Ψ^{-1} are shown as a function of observation nadir, increasing from 0° at the center to 90° at the outer circumference, and relative azimuth (data have been averaged about the principal plane), which increases in a counterclockwise sense from the heading toward the sun. Evident is the typical sunglint pattern with brightest features for views directed toward the nadir. Careful inspection reveals that the innermost contours are not centered in the figure but are shifted slightly toward the azimuth of the sun at 0°, which is consistent with the position of the specular reflection in the pattern.

If these BDR models are applied to data collected by satellite platforms, there are obvious differences to be considered in the spectral responses, the FOV parameters, and the altitude of the measurements. In the following discussion we maintain that the spectral differences are mitigated since the bugeye spectral response includes the region seen by a visible GOES channel, for example, and spatial variation of the radiance signals depends largely upon structural features of the reflecting scene elements to which all portions of the spectrum will respond. Some discussion of the effects of the altitude and FOV features must be considered, and the following is presented to assist the reader in interpreting the results presented below as they apply to operational satellite performance.

From an altitude of 10 km the bugeye samples a circular area at the surface that is approximately 1.75-km diameter at nadir, which is roughly twice as large as the *GOES-8* instantaneous FOV for the 0.52–0.72-μm visible channel. For the off-nadir views, the bugeye FOVs are of course even larger in a relative sense. In what follows, we may envision the bugeye as providing a sampling of the radiance field at points along the aircraft flight track, while at the same time instantaneously viewing radiances arriving from the other detector positions. These data may be used to sample the flux density and, simultaneously, the ''top of the atmosphere'' BDR function, thus providing information on the accuracy of the BDR model for transforming the radiances into the flux density.

The next section provides a method for determination of a minimum distance over which the inference process is valid and presents results for the clear ocean scene. In section 5 convergence analyses are presented for several scenes, indicating errors associated with application of the inference process over various spatial scales.

4. Coherence properties of bidirectional reflectance function

The inference process is examined with emphasis on spatial averaging behavior. This section attempts to determine if there may be a minimum spatial scale below which use of BDR models is not advisable. As previously defined, the inverse of the BDR normalization coefficient is given as $\Psi^{-1}(\theta, \phi) = \pi N(\theta, \phi)/E$, where $N(\theta, \phi)$ is the instantaneous radiance measured at nadir angle θ and relative azimuth angle ϕ and E is the upwelling irradiance; also, $E = \int_\Omega N(\theta, \phi) \cos\theta \, d\Omega$, where Ω represents the solid angle of the upper hemisphere and the dependence on solar zenith angle has been dropped.

The nature of the parameter Ψ is now considered only as a factor in the relation of radiance to irradiance; its angular characteristics are ignored for the present. In fact, it is no longer even necessarilly considered as a constant. This modification is envisioned within the following statistical framework. For a satellite making an inference E_t, after viewing the scene for a time t, from a series of $r + 1$ radiances (N_t, N_{t-1}, . . . , N_{t-r}) (at a particular nadir and relative azimuth that are not explicitly noted), a moving average process is defined—one for which we admit a possibly variable value of Ψ as the detector views various aspects of the scene. In

an ideal scenario, one would like to have the capability to apply a proper Ψ to each pixel of the radiance measurements along the satelllite track to infer the irradiance; however, this is not practical since it would require an extremely large cataloging of BDR models and the ability to identify each of the heterogeneous components making up a complex scene. For a realistic scenario, such as the ''clear'' ocean scene, the detector includes within its FOV some combination of scene elements (clouds, waves, and calmer water). In reality, if the flux density of an extended region is desired, many radiance measurements are required to be averaged, and these are normally used in combination with a single or a few BDR models to achieve the inference. Also, even if the scene were completely void of cloud, changes in Ψ can result from changing surface wind speed or the presence of biological slicks, for example.

The moving average process described above is of a type often analyzed in terms of the cross-covariance statistic between two stochastic signals, as described in Jenkins and Watts (1968). Changing the above notation slightly, we identify the radiance as the input to the process and the flux density as the output according to $E_t = \pi \sum_{r=0}^{M} \Psi_r N_{t-r} + Z_t$, where M is the last point in the average, Ψ now has a reduced magnitude so as to include the $1/(M + 1)$ averaging factor, and Z_t is assumed to be a noise process that accounts for all contributions not predicted by the right-hand-side summation. In this application we consider that the Ψ function consists of $(M + 1)$ values that play the role of a weighting function specifying the impact of each radiance on the scene's moving average. In formulating BDR in this fashion, it is not the intent to explicitly examine the variation of Ψ, but rather to facilitate the analysis of the spatial spectral nature of the inference process in a way that will become clear shortly, enabling one to specify a region for which the BDR has meaning in infering the average scene flux density. In order to do so, the notion of the autocovariance and cross-covariance estimates of the flux density and radiance signals at various time lags are formulated in a procedure leading up to the definition of the squared coherency estimate between the radiance and flux density spectra.

For continuous functions, then, within this statistical framework, the autocovariance of the flux density would be defined as $\gamma_{EE}(u) = \int_{-\infty}^{\infty}\int_{-\infty}^{\infty} \Psi(v)\Psi(u)\gamma_{NN}(u + v - v')\, dv\, dv' + \gamma_{ZZ}(u)$, where, u, v, and v' represent the covariance lags, and γ_{NN} and γ_{ZZ} are the autocovariances of the radiance and noise processes, respectively. Taking the Fourier transform of this expression results in the definition for the autospectrum $\Gamma_{EE}(f)$ of the flux density; $\Gamma_{EE}(f) = G^2(f)\Gamma_{NN}(f) + \Gamma_{ZZ}(f)$, where f is the frequency, $\Gamma_{NN}(f)$ and $\Gamma_{ZZ}(f)$ are the corresponding autospectra of the radiance and noise processes, and $G(f)$ is the expression for the gain of the system. Here $G(f)$ is given by $G(f) = \alpha_{NE}(f)/\Gamma_{NN}(f)$, where $\alpha_{NE}(f)$ is the cross amplitude at frequency f. Without going into a detailed discussion of each of these quantities, the relationship among the autospectra may be written as

$$\Gamma_{EE}(f) - \frac{\alpha_{NE}^2(f)}{\Gamma_{NN}(f)} = \Gamma_{zz}(f).$$

If we define a new quantity, the squared coherency statistic, as

$$\kappa_{NE}^2(f) = \frac{\alpha_{NE}^2(f)}{\Gamma_{NN}(f)\Gamma_{EE}(f)},$$

then we can write the autospectrum of the noise as

$$\Gamma_{ZZ}(f) = \Gamma_{EE}(f)[1 - \kappa_{NE}^2(f)].$$

In the last expression, it is seen that κ_{NE}^2 plays the role of a correlation coefficient in the frequency domain. Thus, when the squared coherency is equal to 0, the noise and flux density spectra are identical at each frequency and there is no correlation between the radiance and the flux density at frequency f. When the squared coherency is near unity, the noise spectra is nearly zero at each frequency, indicating a high degree of correlation at each frequency between the radiance and flux density. Note that a constant BDR function cannot affect the correlation differently at different frequencies.

Herein lies the interest in the squared coherency statistic. Basically, since it defines the amount of correlation between the radiance and irradiance at each frequency, it also contains information about the spatial wavelengths of correlation between the two signals. In this way the analysis provides one criterion for establishing a spatial scale over which the inference process is valid. If the radiance and irradiance signals are not correlated at spatial wavelengths for a given inference geometry, it is difficult to argue that a constant BDR function could provide the necessary adjustment.

The coherency statistic was calculated for the ''clear'' ocean data collected by the bugeye for the 10°–20° solar zenith angle regime using the paired time series of the radiances and the ''pseudoirradiance'' $E_t = \sum_{i=1}^{12} N_{ti} \cos\theta_i$, where θ_i is the nadir angle for the ith detector. The latter was used instead of the Eppley irradiance to avoid introducing unwanted ''noise'' into the process that may be caused by spectral differences between the two instruments, for example. As seen in Fig. 3, the bugeye pseudoirradiance is in excellent agreement with the directly measured irradiance, and using the bugeye inferred irradiance will not alter the conclusions as they impact the true irradiances. The time series were processed using a statistical library routine, the outline of which is included in the appendix.

Figure 4 displays the smoothed, squared spectral coherency estimate for the bugeye radiances collected by detector 1 (viewing the scene at nadir) plotted as a function of spatial scale. The set of frequencies allowed in the analysis is given by $(f_i = 0, i/2L, \ldots, 1/2)$, where L was chosen to have a value of 1000 for this analysis. The choice of L is a matter of trade-offs between in-

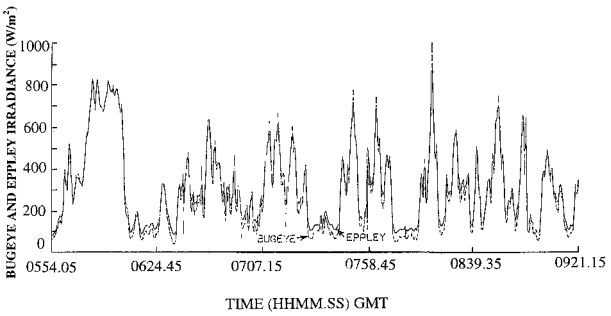

FIG. 3. Comparison of the pseudo–upwelling irradiance calculated from the bugeye data (dashed) and the corresponding irradiance measured with the Eppley pyranometer (solid) collected over broken cloud.

troducing variance in the analysis or bias in the analysis, and the reader is referred to the Jenkins and Watts (1968) text for a detailed discussion of this trade-off. The spatial scale is related to the signal frequency, in this case, through the speed of the aircraft ($v_a = 0.2$ km s^{-1}). Thus, if a cutoff index i_c can be determined as the index of the frequency above which the coherence squared falls below the level of statistical significance, then the cutoff frequency would be given by $f_c = i_c/2000$, and, assuming the scene velocity relative to the aircraft is entirely due to aircraft motion, the wavelength or spatial scale λ_c below which the signals are not spatially correlated would be given by $\lambda_c = v_a/f_c = (0.2)(2000)/i_c$. In Fig. 4 the critical index was identified as $i_c \approx 33$, as discussed below, which results in a critical spatial wavelength of 12 km for this case.

The value of i_c was determined as the frequency index where the statistic falls below a level of 0.833, which is the value of a test statistic below which the coherency squared is not statistically different from 0. The test statistic is determined using the fact that the expression $(v - 2)\overline{K}^2_{12}/2(1 - \overline{K}^2_{12})$ is distributed as $F_{2,v-2}$, where $F_{v1,v2}$ is the Fisher's F distribution with $v1$ and $v2$ degrees of freedom. Thus, at the point that the coherency squared falls below this level in Fig. 4, a vertical line is extended to the spatial scale, indicating that for averaging distances greater than this (approximately 12 km), correlation between radiance and irradiance exists but at smaller scales the statistical test does not support this premise. This analysis was repeated for the other detector signals; however, the results indicated that essentially no remarkable difference exists in the critical spatial scales.

Initially, this test was invoked to find preferred angles to view the various scenes with the thinking that some preferred viewing direction could be found; however, as just mentioned, no great advantage for any particular direction was found for the clear ocean scene. This may not be too surprising when the manner in which the original analysis was performed is considered. The coherency squared statistic involves selecting one of the detector signals against the cosine weighted combination of all the detector readings, including the one selected. In this sense, the analysis is probably more suited for identifying viewing geometries that should be avoided, although none were found for the clear ocean scene. It must also be noted that the instrument was flown typically at an altitude of 12 km, so the spatial scale of 12 km required for spatial coherence occurs at a distance corresponding approximately to the half-angle subtense of a hemispheric detector intercepting half the total incident power. Whether this correspondence is coincidental or consequential has not been determined. Nevertheless, the methodology is suggestive of a means to determine minimum spatial inference scales.

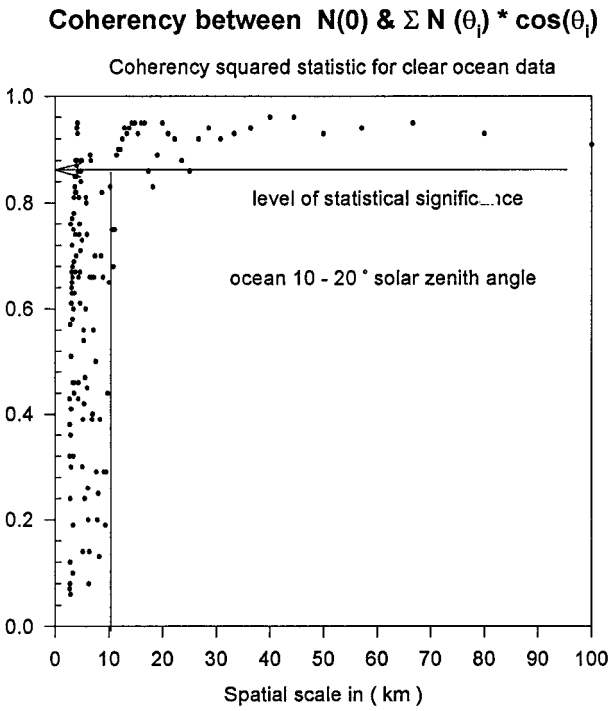

FIG. 4. Squared coherency statistic for the clear ocean data plotted as a function of the spatial scales corresponding to the wavelengths for which it was analyzed. The vertical line is drawn at the point where the coherency falls below the level at which it is statistically different from 0.

Although no preferred view geometry was identified using this analysis, the method is viewed as a means to provide information on quantifying the spatial scales below which instantaneous flux density inference is not statistically valid. While it may be that temporal averaging over a smaller spatial scale provides valid average inferences, use of a scene-averaged BDR function at smaller spatial scales coupled with small temporal scales does not appear to be prudent.

5. Spatial convergence of the inference

While the analysis of the spectral coherence reveals frequencies above which the radiances and irradiances are not correlated, there is no measure of the amount

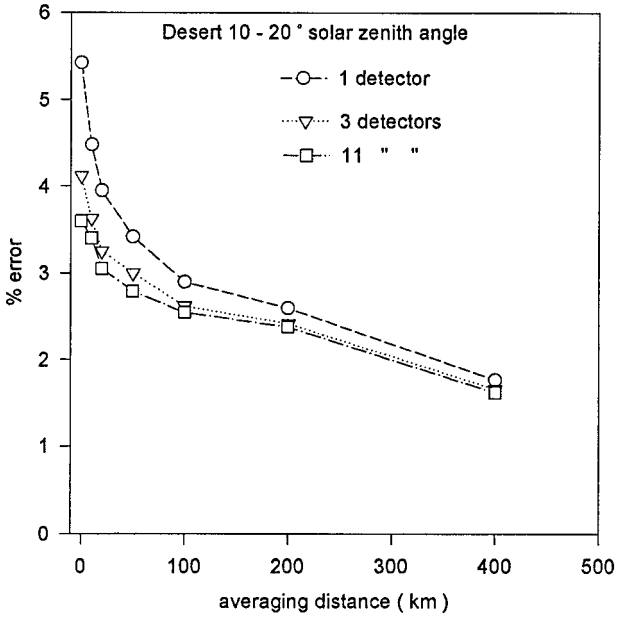

FIG. 5. Percentage error between the scene-averaged pseudo–flux density and the averaged inferred flux density calculated from combinations of detector signals as a function of spatial averaging distance for the desert scene.

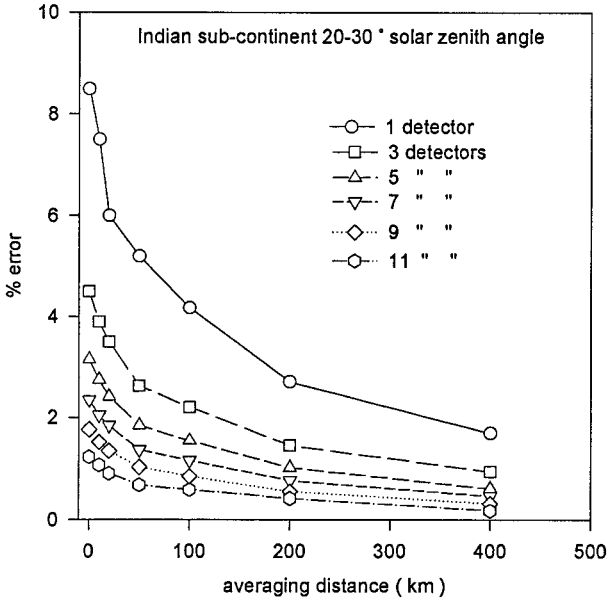

FIG. 6. Percentage error between the scene-averaged pseudo–flux density and the averaged inferred flux density calculated from combinations of detector signals as a function of spatial averaging distance for the Indian subcontinent scene.

of error that this may introduce, nor the error in the inference process at scales at which the signals are correlated. To evaluate the error in the inference that may be anticipated as a function of spatial scale of the inference, the following simple numerical experiment was performed. The experiment was designed to avoid biases due to using a particular viewing geometry. For a particular scene type, which includes specification of the reflecting surface and the solar geometry, a BDR model was created. The BDR model was averaged over the entire region of data collection for a particular scene. Next, for each combination of the $n = 12$ detectors taken r at a time, which number C_r^n, the standard error between the scene averaged pseudoirradiance E_p and the average of r irradiances E_i separately inferred through the use of the BDR was calculated, where r was in the set {1, 3, 5, 7, 9, 11}. Thus, at any point, for the single detector case, E_i represents any single irradiance inferred from the 12 separate radiance measurements; for $r = 3$, E_i is any of 220 averaged inferences made from three radiances each, and so on. The standard percentage error

$$E_r = \frac{100}{E_p} \frac{\sqrt{\sum_{i=1}^{C_r^{12}} (E_i - E_p)^2}}{C_r^{12}}$$

was calculated from all possible combinations of irradiances inferred from r detectors at each spatial point of data collection. Finally, the percentage errors E_r were spatially averaged over distances of 1, 10, 20, 50, 100, 200, and 400 km and plotted as a function of distance.

Figures 5–9 indicate the results of this process for several scenes and show the mean error of inferring irradiance from r observations averaged over various distances. In comparing the spatial convergence, note that this analysis is influenced to some extent by the distance over which the data that compose a particular

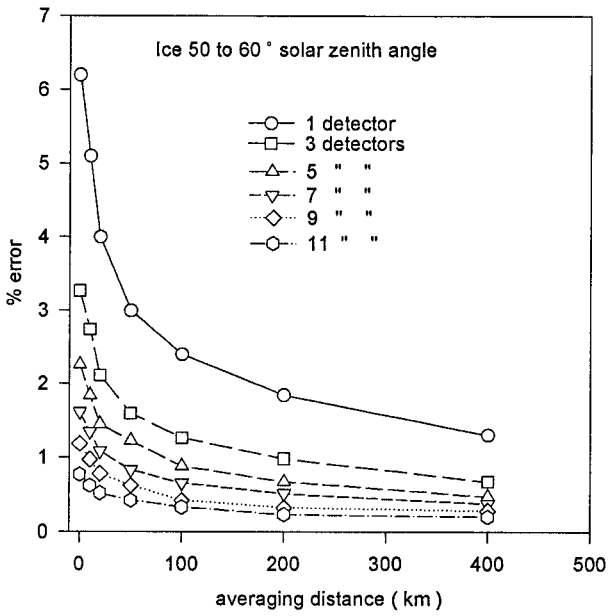

FIG. 7. Percentage error between the scene-averaged pseudo–flux density and the averaged inferred flux density calculated from combinations of detector signals as a function of spatial averaging distance for the sea ice scene.

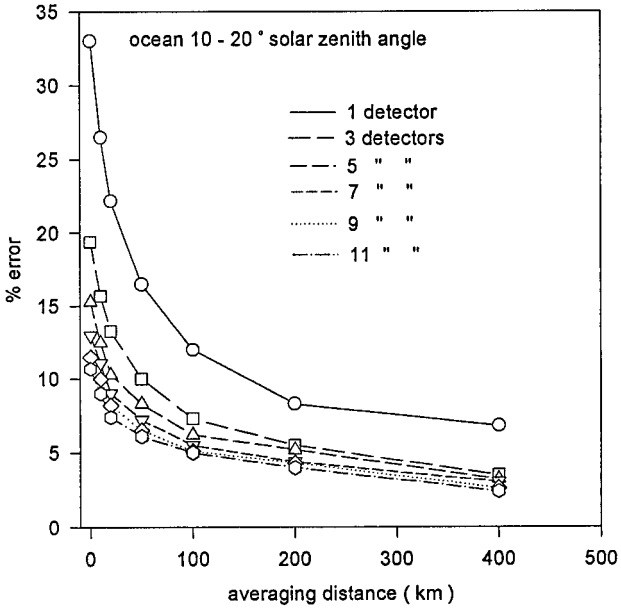

FIG. 8. Percentage error between the scene-averaged pseudo–flux density and the averaged inferred flux density calculated from combinations of detector signals as a function of spatial averaging distance for the clear ocean scene.

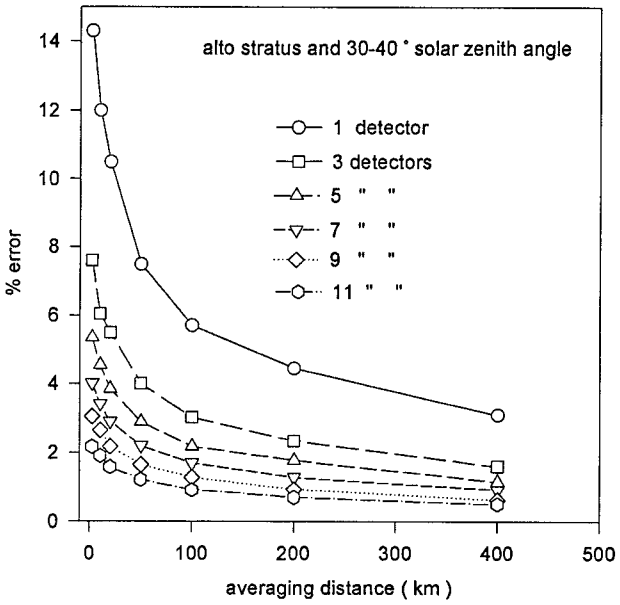

FIG. 9. Percentage error between the scene-averaged pseudo–flux density and the averaged inferred flux density calculated from combinations of detector signals as a function of spatial averaging distance for the altostratus cloud scene.

scene were collected. For example, the equivalent linear distance of the ocean and desert datasets are approximately 1200 km, while the datasets for sea ice, altostratus, and the Indian subcontinent are less than half that size at 600, 500, and 450 km, respectively. Thus, the poorer spatial convergence of the clear ocean data compared to the desert data may have been impacted by the different sample sizes; however, in any operational BDR model there is no guarantee or rationale requiring datasets of equal size. Displayed in this manner the plots show the relative effects of scene anisotropy (amount of decrease in error in utilizing more detectors) and scene inhomogeneity (amount of decrease in error as a function of distance). Contrasting cases may be observed by comparing the plots for the desert case to the others. For example, the desert scene benefits little on a percentage basis for an increase beyond the single detector case (error decrease $< 1\%$) at a 50-km averaging distance, while the error for the altostratus and clear ocean cases continues to decrease even up to seven detector positions for the same averaging distance. It should be noted that the clear ocean scene does contain some cloudiness; however, clouds judged to be resolvable by satellite were filtered from the data. In the ocean data the cloudiness may contribute to the anisotropy, as does the typical sunglint feature, which was not excluded from the analysis.

Although it may appear that Figs. 5–9 indicate that the error in the inference decreases more rapidly with increasing number of detectors than it does with increased averaging distance, it must be emphasized here that the analysis by its nature favors this behavior. This occurs because when the radiance from more than one detector is used in inferring the flux densities, it is the average of the flux density from two or more detectors that is compared to the pseudo–flux density. Thus, it is likely that the average contains both overestimates and underestimates of the inference and that the average of these will cancel each other before the squared differences are summed. On the other hand, the average over distance consists of magnitudes of errors in which there is no corresponding error cancellation. Nevertheless, these analyses may be used to compare the merit of using more than a single detector among scenes and the improvement in the inference with averaging distance from scene to scene.

Not all scene types were analyzed in this manner since for some scenes data were not collected over a large enough region. It was desired to examine the convergence properties on a regional basis, and only datasets that contained enough data to comprise an equivalent linear extent of at least 400 km are presented here. To compare all available scene types in terms of the spatial convergence only, another analysis was performed that basically examined the fraction of the total data required in a running mean process to achieve convergence to within 5% of total sample mean. The following steps were used in the analysis. First, for a particular target scene type, an angular array of average radiances, each normalized by the instantaneous upwelling irradiance, was compiled. This array is thus proportional to the average Ψ^{-1} pattern for the scene in a primitive form (i.e., no averaging about the principal plane was performed).

TABLE 1. Average fraction of data required for convergence to within 5% of scene-averaged BDR function. Also shown are the standard deviations of the convergence fractions and the equivalent linear distance (km) over which the measurements have been collected.

Reflecting surface	Solar zenith angle range (deg)	Fraction of sample required for convergence	Std dev of convergence fraction	Equivalent linear distance (km)
Desert	0–10	0.03	0.04	400
	10–20	0.04	0.06	1100
	20–30	0.03	0.04	700
	30–40	0.09	0.11	1000
	40–50	0.01	0.02	1200
	50–60	0.02	0.03	1000
	60–70	0.04	0.07	675
	70–80	0.04	0.05	500
Himalayas	10–20	0.18	0.20	220
	20–30	0.22	0.21	100
Clear ocean	0–10	0.14	0.14	800
	10–20	0.17	0.19	1200
	20–30	0.21	0.21	1100
	30–40	0.23	0.22	900
	40–50	0.13	0.16	1200
	50–60	0.20	0.18	600
India	0–10	0.09	0.09	250
	10–20	0.13	0.13	275
	20–30	0.05	0.07	450
	30–40	0.04	0.06	400
Altostratus	30–40	0.28	0.23	600
	40–50	0.12	0.14	275
	50–60	0.19	0.20	150
Broken cloud				
	10–20	0.14	0.17	175
	20–30	0.19	0.20	150
	30–40	0.16	0.19	100
	40–50	0.28	0.23	25
Sea ice	50–60	0.03	0.04	500

Next, a running mean analysis was performed for the data elements in each angular bin (for each 10° increment in nadir by 30° in relative azimuth), and the fraction of the data required for the running mean to converge to within 5% of the sample mean was recorded. This process was repeated for 100 random entry points into the data of each angular bin. Finally, an average of these fractions over all angular bins weighted by the number of radiance values in each bin was calculated. The results are presented in Table 1, where the average distance to convergence may be obtained by multiplying the average fraction required for convergence by the equivalent linear distance of data collection presented in the last column. It is proposed that this analysis relates to the minimum spatial averaging distances required for flux density inference over regions characterized by the various reflecting media. If it is found that a certain distance is required for convergence of the BDR to the scene average, it is unlikely that flux densities inferred using the scene-averaged BDR will be representative at a smaller spatial scale, especially since BDR models are not normally applied to the same scene from which they are compiled. The standard deviations of the convergence fractions are also shown in the table, where it is seen that the standard deviations are very close to the means. This is similar to the characteristic of the negative exponential distribution, which is commonly used to model the mean time between failures statistic, to which an analogy may be made to the mean distance until convergence statistic presented here. The results in Table 1 indicate that roughly between 5% and 20% of the radiances for a scene must be included before, on the average, the running mean BDR function approaches within 5% of the scene value.

Table 1 reveals the expected, spatially homogeneous nature of the desert, Indian subcontinent, and sea ice scenes. It might also be expected that the Himalayan scene would be relatively inhomogeneous. It is somewhat disconcerting that the altostratus cloud and broken cloud scenes require such a large fraction of the data for convergence since they also have such large reflectance values. It should be pointed out that the broken cloud scenes selected for the analysis were extremely inhomogeneous, consisting of multiple layers, some clouds penetrating between layers with the ocean visible in broken patches below. Nevertheless, the data suggest that inference of flux density over small regions of less than 30–50 km in cloudy conditions may not be advisable. The clear ocean scene is also notably inhomogeneous in nature. This fact may not be as evident from examination of satellite imagery as it is from observations of the surface features from high-altitude aircraft. Although scenes characterized by small-scale clouds (those estimated to be below satellite resolution) were included in the analysis, it is believed that the ocean's slower tendency to convergence was also affected by more subtle changes over the ocean surface, such as changing wave height features and biological slicks that were clearly visible from the CV-990.

The results of this section point to the fact that caution should be used in attempting to infer flux densities over small spatial scales, especially if it is realized that the BDR functions used in the inference have been compiled from large datasets, even if they have been carefully stratified into complex scene types. Both the analyses discussed in the last two sections point out the relatively slow convergence toward a scene-averaged flux density when inferred from radiance measurements using a BDR model.

6. Summary

Multiple angle radiance data collected during the Summer Monsoon Experiment have been used to study the spatial convergence properties of the radiance to irradiance inference process. The coherence squared statistic was applied to the clear ocean data to find spatial frequencies where the radiance and ir-

radiance began to be correlated, thus establishing a scale below which the inference process may not be applicable. A minimum spatial scale of approximately 12 km was found from these data. The radiances were used to compile average bidirectional reflectance models for various scenes, over spatial scales of 400 km or greater, from which it was possible to study the convergence of the inference process. Error in the inference of the regional irradiances was calculated as a function of the scale over which the inferences were averaged and as a function of the number of view perspectives included in the inference. The inference process was examined for preferred view directions in terms of convergence; however, almost no angular preference was found in these data.

Acknowledgments. The original collection and analysis of the bugeye data was supported by the National Science Foundation under Grants ATM-78-12631 and ATM-80-10691. The recent data analysis was sponsored by the National Aeronautics and Space Administration, Contract Number NAG 1-1704, and by the Office of Naval Research, Contract Number N00014-91-J-1422.

APPENDIX

Procedure for Calculating the Squared Coherency Statistic

The following is a description of a numerical algorithm given in Jenkins and Watts (1968) for calculation of the smoothed squared coherency estimate. The notation has been only slightly changed from the original in order to conform to the symbols used above. In what follows, the subscript (E) refers to E_t, the flux density computed from the summation of the cosine weighted bugeye radiances N_t, which are referred to by the subscript (N). Note that the symbol L is used to represent the upper limit of the lag index ($L-1$), as well as the smoothed quadrature spectral estimate. In the original application of this algorithm, ($L-1$) had a value of 999, M for the 10°–20° ocean was 6000, and a rectangular spectral window was used. Thus the smoothed spectral estimates were calculated at frequencies[1] of 0, 1/(2L), . . . , 1/2 Hz. The calculation of the smoothed squared coherency estimate $\overline{\kappa}_{NE}$ proceeds as follows.

1) For the flux density data,

(a) the autocovariance function estimate at lag k is given by

$$C_{EE}(k) = \frac{1}{M}\sum_{t=1}^{M-k}(E_t - \overline{E})(E_{t+k} - \overline{E}),$$
$$0 \le k \le L-1,$$

where

$$\overline{E} = \frac{1}{M}\sum_{t=1}^{M} E_t;$$

(b) the smoothed spectral estimate at frequency i is given by

$$\overline{C}_{EE}(i) = 2\left[c_{EE}(0) + 2\sum_{k=1}^{L-1} c_{EE}(k)w(k)\cos\frac{\pi ki}{L}\right],$$
$$0 \le i \le L,$$

for which $w(k)$ is the value of the spectral window shape at lag k.

2) For the radiance data,

(a) the autocovariance estimate at lag k is given by

$$c_{NN}(k) = \frac{1}{M}\sum_{t=1}^{M-k}(N_t - \overline{N})(N_{t+k} - \overline{N}),$$
$$0 \le k \le L-1,$$

where

$$\overline{N} = \frac{1}{M}\sum_{t=1}^{M} N_t;$$

(b) the smoothed spectral estimate at frequency i is calculated as

$$\overline{C}_{NN}(i) = 2\left[c_{NN}(0) + 2\sum_{k=1}^{L-1} c_{NN}(k)w(k)\cos\frac{\pi ki}{L}\right],$$
$$0 \le i \le L.$$

3) For the E_t and N_t data,

(a) the cross-covariance estimate at lag k is calculated as

$$c_{NE}(k) = \frac{1}{M}\sum_{t=1}^{M-k}(N_t - \overline{N})(E_{t+k} - \overline{E}),$$
$$0 \le k \le L-1,$$

and

$$c_{NE}(-k) = \frac{1}{M}\sum_{t=1}^{M-k}(N_{t+k} - \overline{N})(E_t - \overline{E}),$$
$$0 \le k \le L-1;$$

(b) the even and odd cross-covariance estimates

[1] It is noted that in Jenkins and Watts (1968) it is recommended that the frequencies of the smoothed spectral estimates be set at 0, 1/2F, . . . , 1/2 Hz, where F is of the order of two to three times L; however, this recommendation was not followed in the numerical routine where essentially $F = L$. The recommendation that F be larger than L allows inspection of the covariance plots at a finer frequency resolution, which is helpful in plotting and interpolation but is not expected to affect the conclusions of this research.

$$l_{\mathrm{NE}}(k) = \frac{1}{2}[c_{NE}(k) + c_{NE}(-k)], \qquad 0 \le k \le L-1,$$

and

$$q_{NE}(k) = \frac{1}{2}[c_{NE}(k) - c_{NE}(-k)], \qquad 0 \le k \le L-1;$$

(c) the smoothed co- and quadrature spectral estimates

$$\overline{L}_{NE}(i) = 2\left[l_{NE}(0) + 2\sum_{k=1}^{L-1} l_{NE}(k)w(k)\cos\frac{\pi ik}{L}\right], \qquad 0 \le i \le L,$$

$$\overline{Q}_{NE}(i) = 4\sum_{k=1}^{L-1} q_{NE}(k)w(k)\sin\frac{\pi ik}{L}, \qquad 1 \le i \le L-1,$$

and

$$\overline{Q}_{NE}(0) = \overline{Q}_{NE}(L) = 0;$$

(d) the smoothed cross-amplitude spectral estimate

$$\overline{A}_{NE}(i) = [\overline{L}^{\,2}_{NE}(i) + \overline{Q}^{\,2}_{NE}(i)]^{1/2} \qquad 0 \le i \le L;$$

(e) the smoothed phase spectral estimate

$$\overline{F}_{NE}(i) = \arctan\left[-\frac{\overline{Q}_{NE}(i)}{\overline{L}_{NE}(i)}\right], \qquad 0 \le i \le L;$$

and (f) the smoothed squared coherency spectral estimate

$$\overline{K}^{\,2}_{NE}(i) = \frac{\overline{A}^{\,2}_{NE}(i)}{\overline{C}_{NN}(i)\overline{C}_{EE}(i)}, \qquad 0 \le i \le L.$$

REFERENCES

Bartman, F. L., 1968: Earth reflectance patterns measured by radiometer on high altitude balloon flights. Tech. Rep. 05863-13-T, NASA Contract NASr-564(03), Michigan University, Ann Arbor, MI, 15 pp.

Davis, J. M., and S. K. Cox, 1982: Reflected solar radiances from regional scale scenes. *J. Appl. Meteor.*, **21,** 1698–1712.

Jenkins, G. M., and D. G. Watts, 1968: *Spectral Analysis and Its Applications.* Holden-Day, 525 pp.

Minnis, P., and E. F. Harrison, 1984: Diurnal variability of regional cloud and clear-sky radiative parameters derived from GOES data. Part I: Analysis method. *J. Climate Appl. Meteor.*, **23,** 993–1011.

Salomonson, V. B., and W. E. Marlatt, 1968: Anisotropic solar reflectance over white sand, snow, and stratus clouds. Atmospheric Science Paper 120, Dept. of Atmospheric Science, Colorado State University, 41 pp. [Available from Department of Atmospheric Science, Colorado State University, Fort Collins, CO 80523.]

Suttles, J. T., and Coauthors, 1988: *Reflected Radiation.* Vol. 1. *Angular Radiation Models for Earth-Atmosphere System*, NASA, 147 pp.

Wielicki, B. A., R. D. Cess, M. D. King, D. A. Randall, and E. F. Harrison, 1995: Mission to Planet Earth: Role of clouds and radiation in climate. *Bull. Amer. Meteor. Soc.*, **76,** 2125–2152.